

MASS – METALLICITY RELATION AND FUNDAMENTAL METALLICITY RELATION OF METAL-POOR STAR-FORMING GALAXIES AT $0.6 < Z < 0.9$ FROM THE EBOSS SURVEY

YULONG GAO,^{1,2} MIN BAO,^{3,*} QIRONG YUAN,³ XU KONG,^{1,2} HU ZOU,⁴ XU ZHOU,⁴ YIZHOU GU,³ ZESEN LIN,^{1,2}
 ZHIXIONG LIANG^{1,2} AND CHI HUANG^{1,2}

¹*CAS Key Laboratory for Research in Galaxies and Cosmology, Department of Astronomy, University of Science and Technology of China, Hefei 230026, China*

²*School of Astronomy and Space Science, University of Science and Technology of China, Hefei 230026, China*

³*Department of Physics and Institute of Theoretical Physics, Nanjing Normal University, Nanjing 210023, China; yuanqirong@njnu.edu.cn*

⁴*Key Laboratory of Optical Astronomy, National Astronomical Observatories, Chinese Academy of Sciences, Beijing 100012, China*

ABSTRACT

The stellar mass-metallicity relation ($M_{\star} - Z$, MZR) indicates that the metallicities of galaxies increase with increasing stellar masses. The fundamental metallicity relation (FMR) suggests that the galaxies with higher star formation rates (SFRs) tend to have lower metallicities for a given stellar mass. To examine whether the MZR and FMR still hold at poorer metallicities and higher redshifts, we compile a sample of 35 star-forming galaxies (SFGs) at $0.6 < z < 0.9$ using the public spectral database (v5_10_0) of emission-line galaxies from the extended Baryon Oscillation Spectroscopic Survey (eBOSS). These galaxies are identified for their significant auroral $[\text{O III}]\lambda 4363$ emission line ($\text{S/N} \geq 3$). With the electronic temperature metallicity calibration, we find nine SFGs are extremely metal-poor galaxies with $12 + \log(\text{O/H}) \leq 7.69$ ($1/10 Z_{\odot}$). The metallicity of the most metal-deficient galaxy is 7.35 ± 0.09 (about $1/20 Z_{\odot}$). Compared with the SFGs with normal metallicities in local and high redshift universe, our metal-poor SFGs have more than ten times higher SFRs at a fixed stellar mass. We create a new mass – SFR relation for these metal-poor galaxies at $0.6 < z < 0.9$. Due to the higher SFRs and younger stellar ages, our metal-poor SFGs deviate from the MZR and FMR in the local universe toward lower metallicities, confirming the existence of FMR, as well as the cosmic evolution of MZR and FMR with redshift.

Keywords: galaxies: abundances — galaxies: distance and redshifts — galaxies: evolution — galaxies: ISM — galaxies: photometry — galaxies: starburst

* Yulong Gao and Min Bao contributed equally to this work.

1. INTRODUCTION

The gas-phase heavy-element abundance in the interstellar medium (ISM), known as “metallicity”, is a fundamental quantity that reflects the evolutionary stage of galaxies. The metallicity of a galaxy has been influenced by a lot of key processes in galaxy formation that remains to be deeply understood. The metal content within a galaxy seems to be primarily set by metal enhancement by star formation, but diluted in the short-term by the cosmological gas inflow and ejected by large-scale outflow via galactic winds (e.g., Dalcanton 2007; Davé et al. 2011; Lilly et al. 2013). The inflowing gas provides the raw fuel for star formation on a longer timescale, while the galactic outflow enriches the ISM and inflowing gas. The baryons are cycling in and out of galaxies and may lead to a direct impact on the stellar masses (M_*), metallicities (Z), and star formation rates (SFRs) of the galaxies. For this reason, the stellar mass-metallicity relation (MZR), the “main sequence” relation (MSR) between galaxy SFRs and stellar masses, and the fundamental metallicity relation (FMR, M_* – SFR – Z) may serve as observational constraints on models of galaxy evolution, which provides a better understanding of the build-up of galaxies across cosmic time.

The MZR, established by Lequeux et al. (1979) and developed by a series of studies (e.g., Tremonti et al. 2004; Mannucci et al. 2010; Andrews & Martini 2013), indicates a trend that the metallicities of galaxies increase with increasing stellar masses. Mannucci et al. (2010) and Andrews & Martini (2013) found that metallicity has an anti-correlation with SFR at a given stellar mass, and constructed the M_* – SFR – Z relation (or FMR). However, Sánchez et al. (2013) and Barrera-Ballesteros et al. (2017) argued that MZR is independent on the SFR. In addition, the evolution of MZR with redshift has also been explored for years (e.g., Savaglio et al. 2005; Maiolino et al. 2008; Zahid et al. 2011; Yuan et al. 2013; Lian et al. 2015; Ly et al. 2016b), since the larger telescopes and deeper spectroscopic surveys. These studies suggested the existence of cosmic evolution for MZR, which means that galaxies at higher- z universe tend to have lower metallicity at a fixed stellar mass.

There are a variety of methods to determine the metallicity (Kewley & Ellison 2008). Some calibrations are based on the photoionization models for H II regions by reproducing some emission line ratios, like $([O\,II]\lambda 3727 + [O\,III]\lambda\lambda 4959, 5007)/H\beta$ (R23, Kobulnicky & Kewley 2004), $[N\,II]\lambda 6583/[O\,II]\lambda 3727$ (N2O2, Kewley & Dopita 2002). Some other calibrations are empirical fits to the electronic temperature (T_e) method

with strong-line ratios for H II regions and galaxies, like $([O\,III]\lambda 5007/H\beta)/([N\,II]\lambda 6583/H\alpha)$ and $[N\,II]\lambda 6583/H\alpha$ (O3N2, N2, Pettini & Pagel 2004). However, there are some problems when using these strong-line metallicity calibrations. For example, the MZRs with different calibrations have different shapes and normalization values (Kewley & Ellison 2008). For high- z star-forming galaxies, these calibrations may not be valid, since their physical conditions (e.g., gas density, ionization, N/O abundance) of the interstellar gas are significantly different from those in local universe (Ly et al. 2016b).

The metallicity calibration with the electronic temperature of ionized gas, using the $[O\,III]\lambda 4363/[O\,III]\lambda 5007$ ratio, which is also called T_e method (Aller 1984), is considered as the most reliable approach to determine the gas-phase oxygen-to-hydrogen (O/H) abundance (Izotov et al. 2006). The weak $[O\,III]\lambda 4363$, produced by H II regions with high enough temperature, can only be detected in metal-poor emission line galaxies. For the local universe, some previous studies have made enormous efforts to enlarge the sample size of metal-poor galaxies with T_e -based metallicities (e.g., Izotov et al. 2006; Berg et al. 2012; Izotov et al. 2012; Gao et al. 2017; Hsyu et al. 2018). Izotov et al. (2006) found six new extremely metal-poor galaxies (XMPGs; $12 + \log(O/H) \leq 7.69$) from 310 emission line galaxies (ELGs) with $S/N([O\,III]\lambda 4363) > 2$ in Sloan Digital Sky Survey (SDSS) Data Release (DR) 3 dataset. Berg et al. (2012) also investigated 19 new metal-poor galaxies with $S/N([O\,III]\lambda 4363) > 4$ using the MMT telescope. In the SDSS DR7, Izotov et al. (2012) found seven metal-deficient galaxies with $12 + \log(O/H) \leq 7.35$. Based on the photometric colors and morphologies in SDSS DR12, Hsyu et al. (2018) determined 45 blue compact dwarf galaxies (BCDs) with $12 + \log(O/H) \leq 7.65$. However, the weak $[O\,III]\lambda 4363$ is even harder to detect for galaxies at $z \geq 0.2$. Some studies used large telescopes, such as Keck II, MMT and VLT, to search the metal-poor galaxies with $[O\,III]\lambda 4363$ detection at $0.5 \leq z \leq 1.0$ (e.g., Kakazu et al. 2007; Amorín et al. 2014; Ly et al. 2014, 2015; Ly et al. 2016b). In total, the number of the metal-poor galaxies with $S/N([O\,III]\lambda 4363) \geq 3$ is less than 300.

The metal-poor galaxies play an essential role in understanding the galaxy evolution, especially for the galaxies at the early stage of evolution, or for those evolve slowly. The low metallicities of these galaxies also suggest that they might have significant metal-poor gas inflows or metal-enriched gas outflows. The interstellar medium (ISM) in these galaxies is nearly pristine and could shed light on the ISM properties at the galaxy formation time. Furthermore, because these galaxies lo-

cated in the very early stage of chemical evolution, a large sample of metal-poor galaxies is necessary to improve the determination of primordial ^4He abundance (Izotov & Thuan 2004) predicted by the standard Big Bang nucleosynthesis model.

In this work, we try to search the new metal-poor galaxy candidates at $0.6 < z < 0.9$ by their $[\text{O III}]\lambda 4363$ line from the eBOSS survey, and then explore the cosmic evolution of MZR and FMR with metallicities derived using direct method. In our next work, using the strong-line metallicity calibrations, Huang et al. (2018, in prep) will divide all the ELGs in eBOSS survey into different bin regions, based on stellar mass, SFR and the 4000Å break ($D_n 4000$), to mainly explore the cosmic evolution of MZR and FMR.

This paper is organized as follows. In Section 2, we describe the methodology for detecting and measuring nebular emission lines, the measurements of metallicity and stellar mass, the selection for star-forming galaxies and SFR determination. In Section 3, we provide the results and discussion about the main sequence relation, the MZR and FMR based our metal-poor galaxies. Finally, we present the main results in Section 4. Throughout this paper, we adopt the solar metallicity (Z_\odot) as $12 + \log(\text{O/H}) = 8.69$ (Allende Prieto et al. 2001) and a flat ΛCDM cosmology with $\Omega_\Lambda = 0.7$, $\Omega_m = 0.3$, and $H_0 = 70 \text{ km s}^{-1} \text{ Mpc}^{-1}$.

2. THE DATA ANALYSIS

2.1. The eBOSS Overview

The Extended Baryon Oscillation Spectroscopic Survey (eBOSS, Dawson et al. 2016), one of the three core programs in the SDSS-IV (Blanton et al. 2017), will map the distribution of galaxies and quasars at redshift $z \sim 0.6 - 3.5$ and improve constraints on the nature of dark energy. This survey started in 2014 July and will create the largest volume survey of the universe to date when finished until Spring 2020. eBOSS will target about 300,000 luminous red galaxies (LRGs) over 7500 deg^2 ($0.6 < z < 0.8$), 189,000 ELGs over 1000 deg^2 ($0.6 < z < 1.0$) and 73,000 quasars over 7500 deg^2 ($0.9 < z < 3.5$), and then provide the spectra with coverage of $3600 - 10300\text{\AA}$ at a resolution of $R \sim 2000$. The eBOSS team has delivered a public Value Added Catalogue ¹ (VAC; ‘spAll-v5_10_0.fits’) together with spectral data covering $\sim 2480 \text{ deg}^2$ footprint. These data include all sources observed in the first two years of SDSS-IV operations (Abolfathi et al. 2018). From the 3,008,000 objects in the VAC, we select 345,584 galaxies as the parent sam-

ple based on the following criteria: (1) $z_{\text{warning}} = 0$, (2) $\text{class} = \text{‘GALAXY’}$, (3) $\text{platequality} \neq \text{‘bad’}$ and (4) $0.6 < z < 1.0$.

2.2. Spectral Fitting and Emission-line Measurements

With the spectra of these 345,584 galaxies in hand, we first use the color excess $E(\text{B} - \text{V})$ map of the Milky Way (Schlegel et al. 1998) to correct the Galactic reddening for these spectra. Then we mask out the optical emission lines and reproduce the underlying stellar continuum using STARLIGHT code (Cid Fernandes et al. 2005), adopting the combination of 45 single stellar populations (SSPs) from Bruzual & Charlot (2003) (BC03) model and the Chabrier (2003) initial mass function (IMF). These SSPs consist of 15 ages in the range of 1 Myr – 13 Gyr and three different metallicities (0.01, 0.02, 0.05). After subtracting the stellar continuum from the spectrum, we use the multiple Gaussians profiles to measure the fluxes of emission lines (e.g., $[\text{O II}]\lambda 3727$, $\text{H}\gamma$, $[\text{O III}]\lambda 4363$, $\text{H}\beta$, $[\text{O III}]\lambda\lambda 4959, 5007$) with IDL package MPFIT (Markwardt et al. 2009). We also estimate the signal-to-noise ratios (S/N) for these emission lines following the method in Ly et al. (2014), which determines the flux with

$$\text{Flux} = \sum_{-2.5\sigma_G}^{+2.5\sigma_G} [f(\lambda - l_C) - \langle f \rangle] \times l', \quad (1)$$

and assumes the noise as

$$\text{Noise} = \sigma(f) \times l' \times \sqrt{N_{\text{pixel}}}. \quad (2)$$

Here, σ_G is the Gaussian width, $\langle f \rangle$ and $\sigma(f)$ are the median value and standard deviation of flux densities within 200\AA -wide region of spectral continuum, excluded the skylines and emission lines, respectively. l_C is the center wavelength of emission lines, l' is the spectral dispersion, and $N_{\text{pixel}} = 5\sigma_G/l'$. Finally, we assume the “Case B” recombination model and the Calzetti et al. (2000) reddening formalism to derive the color excesses $E(\text{B} - \text{V})$ and correct the fluxes for these emission lines. We set $E(\text{B} - \text{V})$ to zero if the observed ratio $\text{H}\gamma/\text{H}\beta$ is higher than the intrinsic ratio $(\text{H}\gamma/\text{H}\beta)_0 = 0.468$ (Hummer & Storey 1987).

2.3. Primary Sample Selection

In order to get accurate SFRs with emission line luminosities and reliable metallicities with electronic temperature, we select these spectra with the following criteria: $S/N([\text{O III}]\lambda 4363) \geq 3$, $S/N([\text{O II}]\lambda 3727) \geq 5$, $S/N([\text{O III}]\lambda 5007) \geq 10$ and $S/N(\text{H}\beta) \geq 5$. As a result, we get a subsample of 319 galaxies.

¹ https://data.sdss.org/sas/dr14/eboss/spectro/redux/v5_10_0/

2.4. The Stellar-mass Determination From SED Modeling

Since the coverage of rest-frame spectra in our subsample is very narrow ($< 3000\text{\AA}$), the stellar masses derived by fitting stellar continuum with STARLIGHT code are not credible. We perform the spectral energy distribution (SED) fitting with multi-photometric ($g, r, z, W1(3.4\mu\text{m}), W2(4.6\mu\text{m})$ bands) measurements using the IDL code library FAST developed by Kriek et al. (2009).

Because the magnitude values of z band in SDSS have significant uncertainties, we preferentially collect the MODELFLUX values of $g, r, z, W1, W2$ bands for 158/319 galaxies from the Legacy Surveys² (Lang 2014; Raichoor et al. 2017; Zou et al. 2018). The Legacy Surveys produce an inference model catalog of the sky from a series of optical and infrared imaging data. The MODELFLUX values of g, r, z bands for the rest 161/319 galaxies are collected from the eBOSS VAC Catalogue, while the MODELMAG values of $W1, W2$ bands for 78/161 galaxies are derived by cross-matching with the All WISE Source Catalog (Wright et al. 2010). Besides, we correct the broadband (g, r, z bands) photometry by subtracting the contribution of strong emission lines from our spectroscopic, which has been used in previous studies (e.g., Atek et al. 2011; Pirzkal et al. 2013; Izotov et al. 2014; Ly et al. 2014).

In the SED fitting, we adopt the Chabrier (2003) IMF, the Bruzual & Charlot (2003) stellar templates with four metallicities (0.004, 0.008, 0.02, 0.05) and an exponentially decreasing star formation model $\text{SFR} \propto e^{-t/\tau}$ to synthesize magnitudes. We set the stellar population ages ranging from 0 to 10 Gyr and also assume the Calzetti et al. (2000) reddening formalism allowing $E(B-V)$ to vary from 0.0 to 2.0. Varying the input photometry with their photometric errors, we repeat the SED fitting for 1000 times. The stellar mass and its error are assumed as the median value and one sigma value in the distribution of fitting results. The median and standard deviation of the errors on stellar mass estimation in SED fitting are 0.26 ± 0.18 dex, while the uncertainties in SSP selections and mass-to-light ratio are about 0.28 dex (Section 3.4, in detail) and 0.1 dex (Bruzual & Charlot 2003), respectively.

2.5. T_e -based Metallicity Determination

To determine the gas-phase metallicity for our SFGs with significant detection of $[\text{O III}]\lambda 4363$, we use the T_e method (e.g., Aller 1984; Izotov et al. 2012; Ly et al.

2016a; Bian et al. 2018). In general, one needs to use the $[\text{S II}]\lambda\lambda 6717, 6731$ doublet lines to determine the electron densities (n_e) and the electron temperatures T_e . However, since the $[\text{S II}]$ doublet lines are redshifted out of our spectral coverage, we assume the n_e as 100 cm^{-3} like used in Ly et al. (2014). Same as our previous work (Gao et al. 2017; Lin et al. 2017), we use the python package PYNEB³ developed by Luridiana et al. (2015) to calculate the metallicity. In the calculation process, we set the atomic recombination data and atomic collision strength data for a series of ions ($\text{O}^+, \text{O}^{++}$) (Gao et al. 2017, in detail). We also follow an iterative method in Nicholls et al. (2014) to determine the temperature of O^+ region $T_e([\text{O II}])$ with the temperature of O^{++} region $T_e([\text{O III}])$ and the total oxygen abundance, $12 + \log(\text{O/H})$.

For the uncertainty in metallicity determination, we simulate the emission lines according to the measured fluxes and errors, and repeat the metallicity calculation for 1000 times. We regard the median value of the 1000 measurements as the measurement value, and the one sigma value of the distribution as the error. The median and standard deviation of uncertainties for metallicity are 0.15 ± 0.07 dex.

2.6. Exclusion of AGNs and Final Sample Selection

Due to the absence of the emission lines $\text{H}\alpha$ and $[\text{N II}]\lambda 6583$ for all spectra in the subsample, we exclude the galaxies that harbor active galactic nucleus (AGNs) using the “Mass-extinction” diagram (MEx; Juneau et al. 2011; Trump et al. 2013), instead of the BPT diagram (Baldwin et al. 1981; Kewley et al. 2001; Kauffmann et al. 2003). There are 136/319 galaxies located in the star-forming region. However, taking the T_e -based metallicity in Section 2.5 into consideration, we have 81/136 galaxies with effective metallicities. Then we inspect the spectra of rest 81 galaxies visually, and exclude 9/81 Seyfert galaxies with high ionization lines $[\text{Nev}]\lambda 3425$ and $[\text{He II}]\lambda 4686$ (Izotov et al. 2012; Ly et al. 2014), as well as 37/81 spectra with fake $[\text{O III}]\lambda 4363$ detection or contaminated by OH skylines. Finally, our final SFG sample consists of 35 galaxies.

The sample selection is shown in the Figure 1. All symbols represent the 319 candidates in subsample selected with signal-to-noise of emission lines in Section 2.3. Green and red stars represent the 183 AGNs in MEx-AGN region and nine Seyfert galaxies, respectively. Gray triangles and magenta diamonds show the 55 galaxies without effective metallicities and 37 galaxies with fake $[\text{O III}]\lambda 4363$ detection or contaminated by

² <http://legacysurvey.org/>

³ <http://www.iac.es/proyecto/PyNeb/>

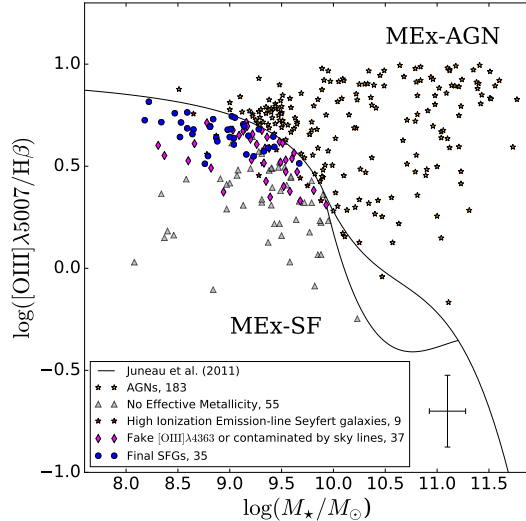


Figure 1. Flux ratio $[\text{O III}]/\text{H}\beta$ as a function of stellar mass (i.e., the MEx diagram). 183 (green stars) and nine (red stars) galaxies are identified as AGNs via the black solid Juneau et al. (2011) demarcation lines and the presence of high ionization lines $[\text{Nev}]\lambda 3425$ and $[\text{He II}]\lambda 4686$, respectively. 37 galaxies (magenta diamonds) are found with fake $[\text{O III}]\lambda 4363$ detection or severely contaminated by OH skylines. Blue filled circles denote the SFG sample. 55 galaxies (gray triangles) have ineffective metallicities. Blue filled circles denote our final SFG sample. The error bar shows the median values of measurement uncertainties for stellar mass and $[\text{O III}]/\text{H}\beta$ ratio.

OH skylines. Blue filled circles denote our final SFG sample. Figure 2 shows the eBOSS spectra for six representative $[\text{O III}]\lambda 4363$ -detected SFGs, which span a rest-frame wavelength range from 3400Å to 5100Å. For each panel, the spectral ID (*plate* – *mjd* – *fiberid*), red-

shift, $\text{S/N}([\text{O III}]\lambda 4363)$ and T_e -based metallicity are also given in the top left. The OH skylines are denoted by the vertical gray shaded bands in the manner, that the darker bands indicate the stronger skylines.

2.7. SFR Estimation From $\text{H}\beta$

In addition to stellar mass and oxygen abundances, we can estimate the dust-corrected SFRs using the $\text{H}\beta$ luminosities $L_{\text{cor}}(\text{H}\beta)$. Assuming a Chabrier (2003) IMF and solar metallicity, the SFR calculated in Kennicutt (1998) can be written as

$$\text{SFR}(M_{\odot}\text{yr}^{-1}) = 4.4 \times 10^{-42} \times (\text{H}\alpha/\text{H}\beta)_0 \times L_{\text{cor}}(\text{H}\beta)(\text{erg s}^{-1}), \quad (3)$$

where the intrinsic ratio $(\text{H}\alpha/\text{H}\beta)_0 = 2.86$. However, for the galaxies with lower metallicities, the SFRs estimated by the Eq.3 will be overestimated since the greater escape of ionizing photons from more metal-poor O star atmospheres. Ly et al. (2016a) gave the metallicity-corrected SFRs as

$$\log(\text{SFR}_{\text{cor}}) = \log(\text{SFR}) + 0.39y + 0.127y^2, \quad (4)$$

where $y = \log(\text{O/H}) + 3.31$.

We summarize the basic information, properties and measurements of the final $[\text{O III}]\lambda 4363$ -detected SFGs selected from eBOSS in Table 1. We find nine SFGs are extremely metal-poor with $12 + \log(\text{O/H}) \leq 7.69$ (i.e., poorer than $1/10 Z_{\odot}$). The metallicity for the most metal-deficient galaxy (ID: 7396-56809-134, $z = 0.68$) is 7.35 ± 0.09 , about $1/20 Z_{\odot}$.

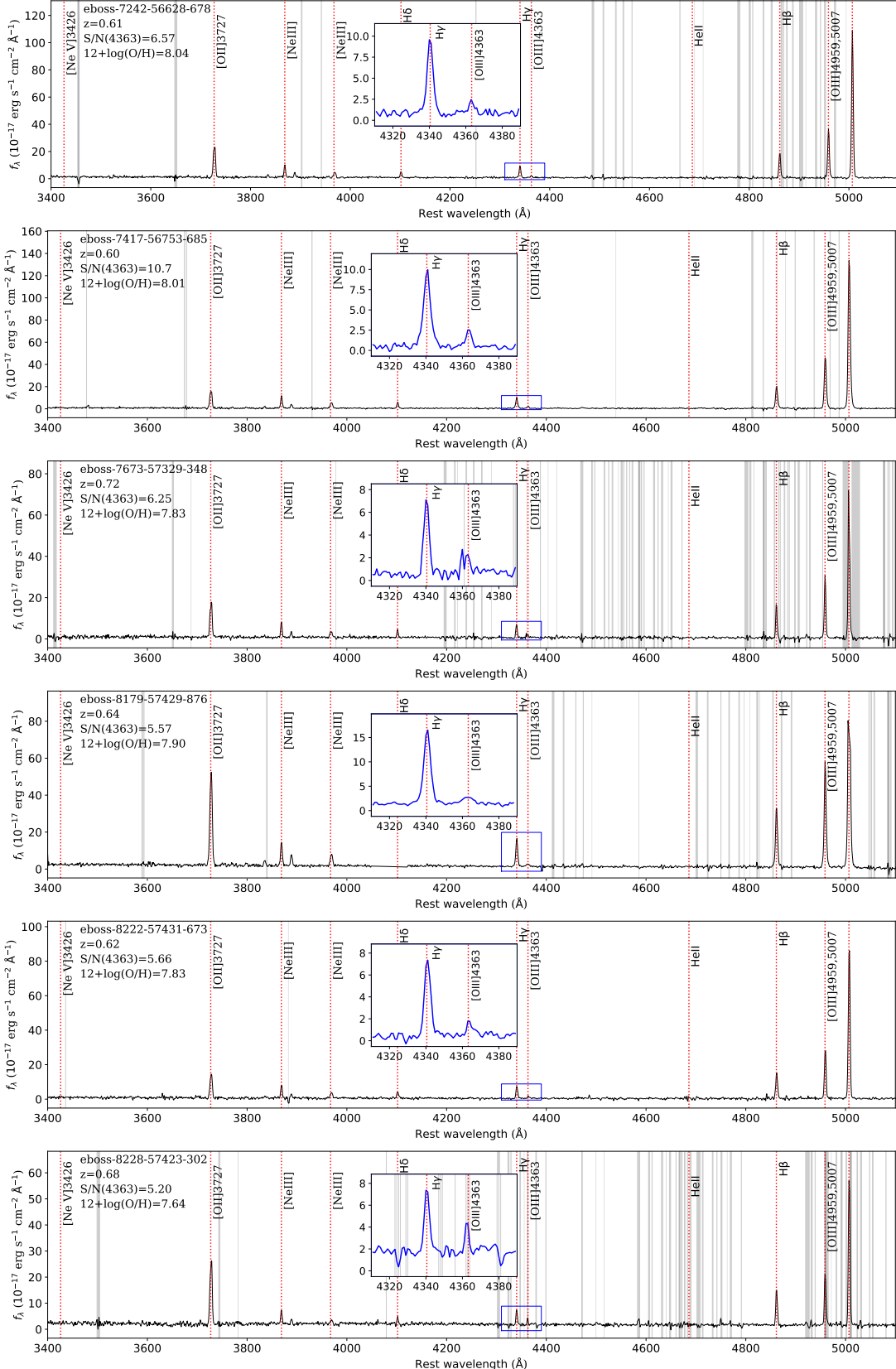


Figure 2. The eBOSS spectra for 6 representative $[\text{O III}]\lambda 4363$ -detected SFGs, which span a rest-frame wavelength range from 3400\AA to 5100\AA , cover the domains of $[\text{Ne V}]\lambda 3425$ to $[\text{O III}]\lambda 5007$. The insets provide a zoomed view of $\text{H}\gamma$ and $[\text{O III}]\lambda 4363$. The spectral ID (*plate - mjd - fiberid*), redshift, $S/N([\text{O III}]\lambda 4363)$ and T_e -based metallicity are also given in the top left. The vertical gray shaded bands denote the OH skylines in the manner that the darker bands indicate the stronger skylines.

Table 1. The properties and measurements of the [O III] $\lambda 4363$ -detected SFGs from eBOSS

ID (plate-mjd-fiberid)	R.A. (deg)	DEC. (deg)	z	$E(B-V)$ (mag)	S/N ($\lambda 4363$)	$D_n 4000$ (\AA)	$\text{EW}(\text{H}\beta)$ ($10^{-17} \text{erg s}^{-1}$)	$\text{H}\beta$ ($10^{-17} \text{erg s}^{-1}$)	$\frac{[\text{O III}]\lambda 5007}{\text{H}\beta}$	$\frac{[\text{O III}]\lambda 5007}{[\text{O III}]\lambda 4363}$	$\log(M_*/M_\odot)$	$\log(\frac{\text{SFR}(\text{H}\beta)}{M_\odot \text{yr}^{-1}})$	$\log(T_e/\text{K})$	$12 + \log(\text{O/H})$
(1)	(2)	(3)	(4)	(5)	(6)	(7)	(8)	(9)	(10)	(11)	(12)	(13)	(14)	(15)
7863-56975-800	3.0797	-1.0267	0.62	0.40 \pm 0.15	3.74	0.90	44.36	335.36 \pm 12.99	3.53 \pm 0.16	49.35 \pm 11.52	9.23 \pm 0.05	1.83 \pm 0.04	4.18 \pm 0.12	7.88 \pm 0.15
7673-57329-348	11.1328	25.6380	0.73	0.17 \pm 0.13	6.26	0.75	107.43	106.90 \pm 5.00	5.38 \pm 0.38	42.53 \pm 18.58	8.84 \pm 0.49	1.50 \pm 0.05	4.22 \pm 0.12	7.84 \pm 0.13
6288-56192-216	13.33805	23.2418	0.77	0.00 \pm 0.15	4.69	0.79	69.74	59.83 \pm 3.48	4.77 \pm 0.43	36.10 \pm 18.75	8.98 \pm 0.47	1.31 \pm 0.06	4.25 \pm 0.15	7.69 \pm 0.16
7241-56606-699	22.6389	21.7292	0.68	0.00 \pm 0.19	3.54	0.79	81.31	27.05 \pm 0.85	5.08 \pm 0.24	48.94 \pm 20.22	9.13 \pm 0.34	0.83 \pm 0.03	4.19 \pm 0.16	7.81 \pm 0.20
7247-56626-567	23.2868	19.3943	0.62	0.23 \pm 0.11	3.52	0.73	86.44	128.37 \pm 2.40	3.93 \pm 0.10	67.19 \pm 10.29	9.43 \pm 0.50	1.41 \pm 0.02	4.13 \pm 0.08	7.97 \pm 0.14
7242-56628-678	23.6418	22.3382	0.61	0.00 \pm 0.09	6.58	0.72	126.87	76.68 \pm 1.28	5.20 \pm 0.12	70.55 \pm 9.46	8.34 \pm 0.45	1.18 \pm 0.02	4.12 \pm 0.05	8.05 \pm 0.07
7248-56630-490	23.9039	18.4817	0.62	0.44 \pm 0.16	3.60	0.91	25.10	203.34 \pm 5.10	3.26 \pm 0.11	26.91 \pm 3.86	9.67 \pm 0.08	1.62 \pm 0.03	4.33 \pm 0.12	7.62 \pm 0.14
5119-55836-950	30.8324	17.0539	0.65	0.00 \pm 0.12	3.67	0.86	69.43	81.03 \pm 1.79	3.61 \pm 0.12	47.84 \pm 10.43	9.16 \pm 0.05	1.26 \pm 0.02	4.19 \pm 0.10	7.81 \pm 0.13
8736-57400-153	31.6903	3.9447	0.73	0.00 \pm 0.15	4.43	0.81	62.09	48.51 \pm 2.44	4.78 \pm 0.29	34.25 \pm 5.25	8.65 \pm 0.06	1.16 \pm 0.05	4.27 \pm 0.07	7.63 \pm 0.12
4261-55503-832	40.4958	3.1851	0.82	0.02 \pm 0.14	4.37	0.70	308.96	63.42 \pm 1.71	4.80 \pm 0.18	36.03 \pm 5.20	9.28 \pm 0.11	1.41 \pm 0.03	4.25 \pm 0.07	7.61 \pm 0.08
8858-57450-666	128.5331	38.5511	0.67	0.27 \pm 0.17	5.69	0.79	83.27	116.07 \pm 1.24	4.95 \pm 0.08	35.64 \pm 2.65	9.14 \pm 0.13	1.45 \pm 0.01	4.26 \pm 0.11	7.73 \pm 0.14
8828-57445-880	130.9153	40.2271	0.73	0.21 \pm 0.12	3.00	0.81	76.28	191.35 \pm 4.31	3.34 \pm 0.13	49.30 \pm 6.89	9.04 \pm 0.35	1.76 \pm 0.02	4.18 \pm 0.08	7.86 \pm 0.13
7315-56685-689	140.7128	46.8123	0.64	0.12 \pm 0.12	4.52	0.80	77.82	97.45 \pm 2.82	4.39 \pm 0.17	47.22 \pm 8.13	8.52 \pm 0.11	1.33 \pm 0.03	4.19 \pm 0.07	7.83 \pm 0.10
7283-57063-843	146.3134	54.8753	0.62	0.11 \pm 0.11	5.30	0.79	82.87	107.48 \pm 1.98	4.55 \pm 0.12	45.56 \pm 5.86	8.64 \pm 0.05	1.34 \pm 0.02	4.20 \pm 0.08	7.82 \pm 0.12
8823-57446-847	148.8682	39.5981	0.83	0.39 \pm 0.12	4.44	0.87	71.88	287.18 \pm 3.33	4.36 \pm 0.08	38.32 \pm 5.30	8.87 \pm 0.32	2.08 \pm 0.01	4.24 \pm 0.14	7.78 \pm 0.14
8853-57459-322	157.7832	35.8713	0.64	0.21 \pm 0.13	4.83	0.61	170.93	116.14 \pm 4.24	4.97 \pm 0.25	34.26 \pm 7.08	8.81 \pm 0.09	1.40 \pm 0.04	4.27 \pm 0.07	7.64 \pm 0.11
8179-57429-876	161.4052	56.7378	0.64	0.00 \pm 0.08	5.58	0.66	141.42	149.42 \pm 3.52	4.19 \pm 0.16	56.69 \pm 9.47	8.88 \pm 0.03	1.52 \pm 0.02	4.16 \pm 0.05	7.91 \pm 0.07
6444-56339-270	162.2911	33.1740	0.77	0.00 \pm 0.14	5.61	0.64	96.97	48.57 \pm 1.79	5.55 \pm 0.28	23.57 \pm 5.80	9.02 \pm 0.28	1.22 \pm 0.04	4.37 \pm 0.14	7.50 \pm 0.17
7396-56809-134	171.9186	45.2847	0.68	0.10 \pm 0.14	6.22	0.85	61.00	75.28 \pm 1.81	3.25 \pm 0.16	34.33 \pm 4.97	8.76 \pm 0.45	1.28 \pm 0.02	4.36 \pm 0.07	7.35 \pm 0.09
7399-57162-661	172.3675	49.3908	0.85	0.00 \pm 0.21	3.84	0.98	69.92	34.42 \pm 2.89	4.04 \pm 0.44	48.84 \pm 36.28	9.04 \pm 0.11	1.18 \pm 0.08	4.19 \pm 0.20	7.83 \pm 0.16
7400-57134-924	175.2757	50.4547	0.68	0.11 \pm 0.11	3.29	0.83	72.34	140.85 \pm 4.90	4.42 \pm 0.22	99.29 \pm 34.21	9.42 \pm 0.44	1.56 \pm 0.03	4.06 \pm 0.09	8.22 \pm 0.12
8230-57430-196	176.7698	54.5643	0.73	0.75 \pm 0.18	3.32	0.75	143.37	1220.27 \pm 3.35	4.81 \pm 0.02	40.63 \pm 0.50	9.01 \pm 0.19	2.57 \pm 0.03	4.22 \pm 0.08	7.93 \pm 0.14
8228-57423-302	178.8998	52.9714	0.68	0.36 \pm 0.14	5.20	0.99	34.67	257.86 \pm 5.57	3.89 \pm 0.12	29.39 \pm 7.41	9.37 \pm 0.14	1.82 \pm 0.02	4.30 \pm 0.16	7.65 \pm 0.20
5979-56329-352	185.5227	23.3482	0.68	0.00 \pm 0.17	3.48	0.74	70.33	39.23 \pm 1.20	4.93 \pm 0.23	47.65 \pm 10.25	8.81 \pm 0.06	1.00 \pm 0.03	4.19 \pm 0.09	7.86 \pm 0.12
6667-56412-226	188.5501	46.6314	0.72	0.24 \pm 0.20	4.27	0.88	89.36	103.67 \pm 2.83	5.18 \pm 0.19	59.93 \pm 17.06	8.53 \pm 0.15	1.49 \pm 0.03	4.15 \pm 0.19	8.01 \pm 0.19
7415-57097-658	190.2230	49.4394	0.69	0.00 \pm 0.11	4.20	0.59	191.21	59.57 \pm 1.52	5.32 \pm 0.19	51.96 \pm 6.53	8.18 \pm 0.04	1.20 \pm 0.03	4.17 \pm 0.05	7.88 \pm 0.09
8211-57423-304	203.3647	50.2998	0.62	0.06 \pm 0.10	5.07	0.87	73.74	110.68 \pm 2.58	3.74 \pm 0.13	56.54 \pm 10.75	9.33 \pm 0.07	1.36 \pm 0.02	4.16 \pm 0.07	7.86 \pm 0.10
7428-56781-95	209.5281	46.1953	0.62	0.21 \pm 0.10	6.11	0.82	99.58	222.14 \pm 6.04	4.39 \pm 0.20	71.50 \pm 13.58	9.00 \pm 0.47	1.65 \pm 0.03	4.11 \pm 0.06	8.05 \pm 0.09
6932-56397-238	214.8633	53.1171	0.60	0.67 \pm 0.19	3.18	0.96	44.84	329.07 \pm 3.65	3.55 \pm 0.05	28.22 \pm 2.14	8.79 \pm 0.20	1.80 \pm 0.01	4.31 \pm 0.15	7.67 \pm 0.19
8498-57105-124	222.6245	39.2227	0.61	0.00 \pm 0.11	4.64	0.83	75.76	84.41 \pm 2.04	4.46 \pm 0.16	85.54 \pm 20.86	9.18 \pm 0.27	1.22 \pm 0.02	4.09 \pm 0.09	8.09 \pm 0.13
3877-55365-528	224.6807	28.8287	0.69	0.04 \pm 0.16	4.23	0.94	41.25	46.80 \pm 1.30	5.75 \pm 0.22	41.35 \pm 9.22	8.47 \pm 0.47	1.09 \pm 0.03	4.22 \pm 0.13	7.83 \pm 0.16
5143-55828-182	322.4144	0.8864	0.72	0.00 \pm 0.17	3.24	0.74	103.87	21.59 \pm 1.17	6.55 \pm 0.48	58.13 \pm 20.80	8.22 \pm 0.45	0.81 \pm 0.05	4.15 \pm 0.12	7.99 \pm 0.11

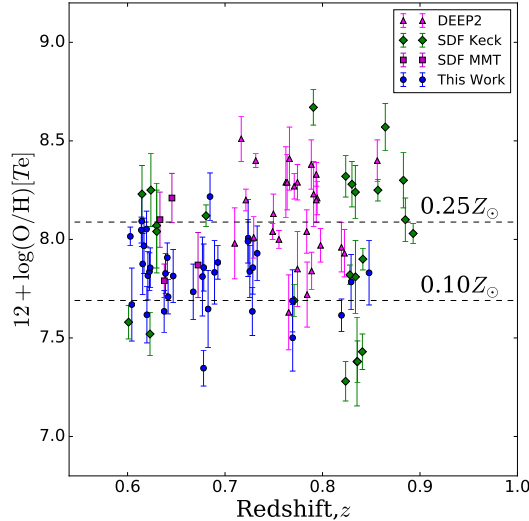


Figure 3. The distributions of T_e -based metallicities and redshifts for some samples of $[\text{O III}]\lambda 4363$ -detected SFGs at $0.6 < z < 0.9$, including 35 SFGs in our eBOSS sample (the blue circles), 28 SFGs from the DEEP2 sample (the magenta triangles) (Ly et al. 2015), 4 SDF MMT/Hectospec sample (the purple squares), and 24 SDF Keck/DEIMOS sample (the green diamonds) (Ly et al. 2016a).

3. RESULTS

3.1. Star-forming Main Sequence

In Figure 3, we show the distributions of T_e -based metallicities versus redshifts for some samples of $[\text{O III}]\lambda 4363$ -detected SFGs at $0.6 < z < 0.9$, including 35 SFGs in our eBOSS sample (the blue circles), 28 SFGs from the DEEP2 sample (the magenta triangles) from Ly et al. (2015), 4 SDF MMT/Hectospec sample (the purple squares), and 24 SDF Keck/DEIMOS sample (the green diamonds) from Ly et al. (2016a). The redshifts of our SFGs span from 0.6 to 0.9. Compared with other samples, most of our SFGs (24/35) are located in $0.6 \leq z \leq 0.7$, while most of the DEEP2 and SDF sample range in $0.7 - 0.9$.

In Figure 4, we plot the metallicity-corrected SFRs derived with $\text{H}\beta$ luminosities as a function of the stellar masses from SED fitting to compare against other metal-poor SFG samples. The symbols are the same as in Figure 3. We also perform the linear fitting for these metal-poor galaxies, and give the best relation as,

$$\log(\text{SFR}/M_{\odot}\text{yr}^{-1}) = 1.24(\pm 0.11) \log(M_{\star}/M_{\odot}) - 10.09(\pm 0.10), \quad (5)$$

shown with solid magenta line. Overlaid as blue and green stripes are the results based on $\text{H}\alpha$ -selected galaxies at $z \sim 0.8$ (de los Reyes et al. 2015) and mass-selected SFGs at $z = 0.5 - 1.0$ (Whitaker et al. 2014), respec-

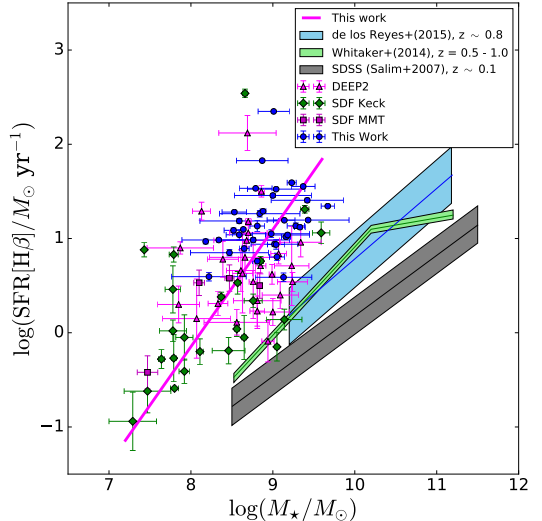


Figure 4. The star-forming main sequence relation for some samples of $[\text{O III}]\lambda 4363$ -detected SFGs at $0.6 < z < 0.9$, which symbols are same as Figure 3. The solid magenta line is the best linear fitting relation for above metal-poor galaxies. Overlaid as blue and green stripes are the results based on $\text{H}\alpha$ -selected galaxies at $z \sim 0.8$ (de los Reyes et al. 2015) and mass-selected SFGs at $z = 0.5 - 1.0$ (Whitaker et al. 2014), respectively. The local star-forming main sequence derived from the SDSS sample of SFGs is also shown in the grey stripe (Salim et al. 2007).

tively. The local star-forming main sequence derived from the SDSS sample of SFGs is also shown in the grey stripe (Salim et al. 2007). The difference between the main sequence relations in local and high redshift universe is also consistent with the result that the rate of declining SFR with redshift is not a strong function of stellar mass (Zheng et al. 2007). Compared with the SFGs with normal metallicities, the metal-poor SFGs in our sample are found to have more intense star formation activities. If extrapolating the M_{\star} – SFR relation to lower M_{\star} , we find the SFRs in our sample are enhanced by 1.0 – 3.0 dex above the M_{\star} – SFR relation in local universe (Salim et al. 2007), and are 0.5 – 2.0 dex higher than the normal SFGs at $z = 0.5 - 1.0$ (Whitaker et al. 2014) or $z \sim 0.8$ (de los Reyes et al. 2015). The coverage of stellar masses and SFRs of our eBOSS SFGs is similar to the DEEP2 sample.

3.2. Stellar Mass – Metallicity Relation

In Figure 5, we plot the relation between gas-phase metallicity and stellar mass (i.e., MZR) for some samples of $[\text{O III}]\lambda 4363$ -detected SFGs at $0.6 < z < 0.9$, including metal-poor SFGs in our eBOSS sample and three other sample, which symbols are same as in Figure 3 and 4. The black solid and dashed lines represent

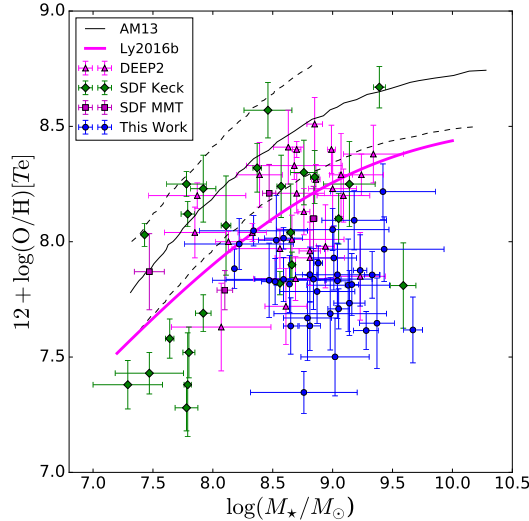


Figure 5. The relation between gas-phase metallicity and stellar mass (i.e., MZR) for some samples of $[\text{O III}]\lambda 4363$ -detected SFGs at $0.6 < z < 0.9$, which symbols are same as in Figure 3. For a direct comparison, the local MZR and its limits derived from the stacked spectra by Andrews & Martini (2013) are given as black solid and dashed lines, while the MZR for SFGs at $0.5 < z < 1.0$ derived by Ly et al. (2016b) is shown as the solid magenta line.

the local MZR and its limits derived from the stacked spectra by Andrews & Martini (2013) based on T_e metallicity calculation, respectively. The solid magenta line represents the MZR for SFGs at $0.5 < z < 1.0$ derived by Ly et al. (2016b). As shown in the figure, most of our eBOSS metal-poor SFGs show lower metallicities than the MZRs in Andrews & Martini (2013) and Ly et al. (2016b) systematically, by about 0.7 dex and 0.3 dex, respectively. Besides, we note that the metallicities in eBOSS SFGs are lower than the metallicities in the DEEP2 sample about 0.37 dex.

In the previous studies, Savaglio et al. (2005) identified a strong correlation between stellar mass and metallicity for 56 galaxies based on R23 method at the high- z universe, and for the first time, found clear evidence for the cosmic evolution of MZR. Lian et al. (2016) also used the R23 method to compare the metallicities of BCDs in local and intermediate- z ($0.2 < z < 0.5$) universe, but did not find a significant deviation in MZR. Determining the metallicities for 66 $[\text{O III}]\lambda 4363$ -detected galaxies with the electron temperature metallicity calibration, Ly et al. (2016b) found the MZR at high redshift have lower metallicities, about 0.25 dex, than the MZR in Andrews & Martini (2013) at all stellar masses. In this work, our SFGs also have systematical lower metallicities than the local MZR, confirming the existence of the cosmic evolution of MZR with redshift. Meanwhile, our

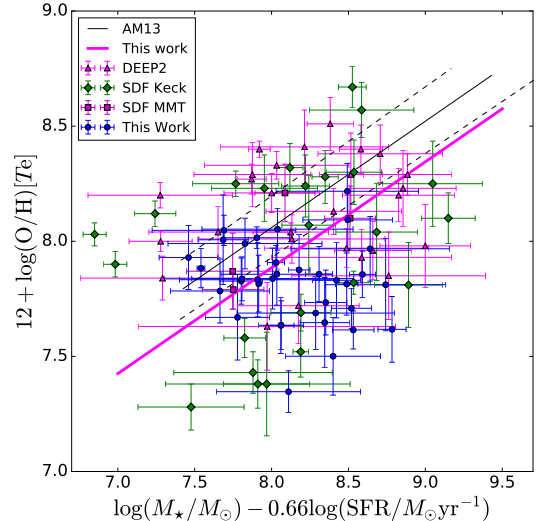


Figure 6. The fundamental metallicity relation (FMR) for some samples of $[\text{O III}]\lambda 4363$ -detected SFGs at $0.6 < z < 0.9$, which symbols are same as in Figure 3. For a direct comparison, the local FMR derived from the stacked spectra by Andrews & Martini (2013) is also given as the black solid and dashed lines. The best FMR relation we fit with the same slope of 0.43 in Andrews & Martini (2013) is shown as the solid magenta line, which has an offset of 0.16 dex below the local FMR.

SFGs also locate below the MZR at $0.5 < z < 1.0$ in Ly et al. (2016b), which may be caused by the higher SFRs, higher stellar masses and/or the uncertainties of stellar mass measurements. Because of the shallow limited-magnitude in eBOSS, these relatively more massive ($8.0 \leq \log(M_*/M_\odot) \leq 9.5$) metal-poor galaxies may be preferably chosen in the sample selection (Izotov et al. 2014).

3.3. Fundamental Metallicity Relation

The stellar mass – SFR – metallicity relation (FMR) is constructed by Mannucci et al. (2010) and Andrews & Martini (2013) to significantly decrease the scatter in MZR, which indicates that the metallicity to be anti-correlated with SFR at a fixed stellar mass. In Figure 6, we show the FMR for some samples of $[\text{O III}]\lambda 4363$ -detected SFGs at $0.6 < z < 0.9$, which symbols are same as in Figure 3, 4 and 5. For a direct comparison, we adopt the SFR coefficient $\alpha = 0.66$ from Andrews & Martini (2013), and give the local FMR with its limits as the black solid and dashed lines. We can find that 10/35 of our metal-poor SFGs can be well fitted by the local FMR within a deviation of 0.14 dex, while the other 25/35 SFGs have the metallicities below the local FMR with an average value 0.43 dex. Furthermore, we also use the linear relation with the same slope of 0.43 in Andrews & Martini (2013) to fit all these data, and find

the best relation (shown as the solid magenta line) has an offset of about 0.16 dex below the local FMR, with a dispersion (standard deviation of the residuals) about 0.32 dex.

Our results confirm the existence of FMR, which means that the metal-poor galaxies with higher SFRs have lower metallicities at a same stellar mass. The offset of FMR also indicates the trend that, similar to MZR cosmic evolution, FMR evolves toward lower metallicity at a fixed stellar mass and SFR in the earlier universe. We note that our SFGs have smaller $D_{\text{n}4000}$ indices ($0.5 \leq D_{\text{n}4000} \leq 1.0$) with a median value of 0.8. The cosmic evolution of FMR may be caused by the fact that SFGs at intermediate- z and high- z have much younger stellar populations than those in the local universe. This result is consistent with the result in Lian et al. (2015) that galaxies with smaller $D_{\text{n}4000}$ typically have lower metallicity at a fixed stellar mass, suggesting that the galaxy stellar age plays an essential role in the MZR and FMR for high-redshift SFGs.

3.4. Discussion for Metallicity and Stellar Mass Determinations

In the process to determine the metallicity with electron temperature, we usually need the $[\text{S II}]\lambda 6717/[\text{S II}]\lambda 6731$ ratio to estimate the electron density n_e , and then use the $[\text{O III}]\lambda\lambda 4959, 5007/[\text{O III}]\lambda 4363$ and n_e to determine the $T_e([\text{O III}])$. However, we note that the n_e effect on metallicity becomes obvious only at $n_e > 10^4 \text{ cm}^{-3}$. If we assume the $n_e = 1,000 \text{ cm}^{-3}$, the metallicities of the SFGs in our sample have a slight offset, about 0.02 dex above those with $n_e = 100 \text{ cm}^{-3}$. As to the $T_e([\text{O III}])$ determination, the $T_e([\text{O II}])$ can be derived with $[\text{O II}]\lambda 3727/[\text{O II}]\lambda\lambda 7320, 7330$ ratio. Due to the absence of $[\text{O II}]\lambda\lambda 7320, 7330$ in our spectra, we follow the method in Nicholls et al. (2014) to determine the $T_e([\text{O II}])$. If calculating the metallicities using the $T_e([\text{O II}]) - T_e([\text{O III}])$ relation from Izotov et al. (2012) and Andrews & Martini (2013), we will yield higher $T_e([\text{O II}])$ values with an average offset about 0.03 dex, which will result in lower metallicities about 0.05 dex.

In order to make a direct comparison with the metal-poor SFGs selected from SDF and DEEP2 surveys, we assume the Chabrier (2003) IMF and Bruzual & Charlot (2003) SSPs, just following Ly et al. (2014) and Ly et al. (2016a), to estimate the stellar masses. However, different assumptions on IMFs and SSPs will lead to some difference in the stellar mass determination (e.g., Bruzual & Charlot 2003; Brinchmann et al. 2008; Parikh et al. 2018). In Figure 7, we show the comparison of stellar mass determination with two different SSP libraries (Bruzual & Charlot 2003; Maraston 2005) and three

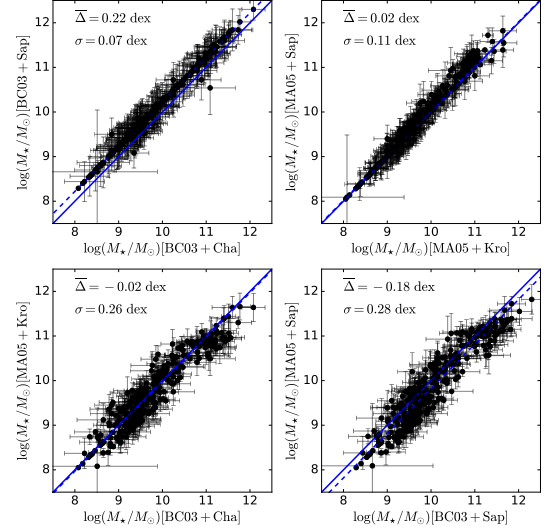


Figure 7. The comparison of stellar mass determination with different SSP libraries and IMFs for the subsample of 319 galaxies selected in Section 2.3. The Bruzual & Charlot (2003) and Maraston (2005) libraries are shown as BC03 and MA05, the Chabrier (2003), Kroupa (2001) and Salpeter (1955) IMFs are abbreviated as Cha, Kro and Sap, respectively. The blue solid lines indicate equality between the stellar masses derived with different parameters. The median values ($\bar{\Delta}$, offset, also shown as blue dashed lines) and the standard deviation (σ) of residuals are also shown in the legends.

IMFs (Salpeter 1955; Kroupa 2001; Chabrier 2003) for the subsample of 319 galaxies selected in Section 2.3. If using the Bruzual & Charlot (2003) SSPs, we note that the stellar masses estimated by Salpeter (1955) IMF have a systematical offset about 0.22 dex above these by Chabrier (2003) IMF, consistent with Sánchez et al. (2016), while have a smallest dispersion about 0.07 dex. If we adopt the Salpeter (1955) IMF, the offset between stellar masses with Bruzual & Charlot (2003) and Maraston (2005) SSPs is about -0.18 dex, and the dispersion is about 0.28 dex. However, as Bruzual & Charlot (2003) pointed out, the Chabrier (2003) IMF is physically motivated, and it shows a better fitting to the counts of low-mass stars and brown dwarfs in the Galactic disc. Compared with the Chabrier (2003) IMF, Salpeter (1955) IMF leads to a systematical overestimation of stellar mass. In brief, the different assumptions in metallicity calibration and mass determination will have a nearly nonsignificant effect on the MZR and FMR for our metal-poor SFGs in eBOSS.

4. SUMMARY

In this work, we use the spectroscopic data of eBOSS in SDSS DR14 dataset to search the metal-poor galaxies with $[\text{O III}]\lambda 4363$ detection at $0.6 < z < 0.9$, and

to explore the cosmic evolution of MZR and FMR. We have determined the metallicity with electron temperature method based on $[\text{O III}]\lambda 4363/[\text{O III}]\lambda 5007$ ratio. The stellar masses are derived from the SED fitting with multi-photometric measurements, and the SFRs are estimated from the $\text{H}\beta$ luminosities. The primary results are summarized as follows.

- We select a sample of 35 metal-poor star-forming galaxy candidates with $\text{S/N}([\text{O III}]\lambda 4363) \geq 3.0$ and has a median value of $12 + \log(\text{O/H}) = 7.83$ in range from 7.35 to 8.22 (Figure 3). Nine SFGs are found to be extremely metal-poor with $12 + \log(\text{O/H}) \leq 7.69$, in which the most metal-deficient galaxy is 7.35 ± 0.09 , about $1/20 Z_\odot$.
- We find the SFRs of our SFGs are enhanced by 1.0 – 3.0 dex above the M_\star – SFR relation (Salim et al. 2007) in local universe (Figure 4). Based on a few of metal-poor galaxy samples, we create a new M_\star – SFR relation for these galaxies at $0.6 \leq z \leq 0.9$, shown as Equation 5.
- Our SFGs have systematical lower metallicities than the local MZR in Andrews & Martini (2013), confirming the existence of the cosmic evolution of MZR with redshift reported in previous studies (Figure 5). Furthermore, we also find the metallicities of these metal-poor SFGs have a systematical offset about 0.16 dex below the local FMR (Figure 6), indicating that galaxies have lower metallicities at a fixed stellar mass and SFR in the earlier universe.

We attribute the cosmic evolution of FMR to the stellar age of galaxies at different redshifts (Section 3.3). In our next work, we will stack the spectra, for all ELGs in the eBOSS survey, in bins of stellar mass, SFR and $D_{\text{n}4000}$, to significantly enhance the S/N of emission lines, and then mainly explore the cosmic evolution of MZR and FMR.

We thank the referee for his/her thorough reading and valuable suggestions. This work is supported by the National Natural Science Foundation of China (NSFC, Nos. 11873032, 11173016, 11320101002, 11421303, and 11433005), the Research Fund for the Doctoral Program of Higher Education of China (Nos. 20133207110006), and the National Key R&D Program of China (2015CB857004, 2016YFA0400702, 2017YFA0402600).

Funding for the Sloan Digital Sky Survey IV has been provided by the Alfred P. Sloan Foundation, the U.S.

Department of Energy Office of Science, and the Participating Institutions. SDSS acknowledges support and resources from the Center for High-Performance Computing at the University of Utah. The SDSS web site is www.sdss.org.

The Legacy Surveys consist of three individual and complementary projects: the Dark Energy Camera Legacy Survey (DECaLS; NOAO Proposal ID # 2014B-0404; PIs: David Schlegel and Arjun Dey), the Beijing-Arizona Sky Survey (BASS; NOAO Proposal ID # 2015A-0801; PIs: Zhou Xu and Xiaohui Fan), and the Mayall z-band Legacy Survey (MzLS; NOAO Proposal ID # 2016A-0453; PI: Arjun Dey). DECaLS, BASS and MzLS together include data obtained, respectively, at the Blanco telescope, Cerro Tololo Inter-American Observatory, National Optical Astronomy Observatory (NOAO); the Bok telescope, Steward Observatory, University of Arizona; and the Mayall telescope, Kitt Peak National Observatory, NOAO. The Legacy Surveys project is honored to be permitted to conduct astronomical research on Iolkam Du’ag (Kitt Peak), a mountain with particular significance to the Tohono O’odham Nation.

NOAO is operated by the Association of Universities for Research in Astronomy (AURA) under a cooperative agreement with the National Science Foundation.

This project used data obtained with the Dark Energy Camera (DECam), which was constructed by the Dark Energy Survey (DES) collaboration. Funding for the DES Projects has been provided by the U.S. Department of Energy, the U.S. National Science Foundation, the Ministry of Science and Education of Spain, the Science and Technology Facilities Council of the United Kingdom, the Higher Education Funding Council for England, the National Center for Supercomputing Applications at the University of Illinois at Urbana-Champaign, the Kavli Institute of Cosmological Physics at the University of Chicago, Center for Cosmology and Astro-Particle Physics at the Ohio State University, the Mitchell Institute for Fundamental Physics and Astronomy at Texas A&M University, Financiadora de Estudos e Projetos, Fundacao Carlos Chagas Filho de Amparo, Financiadora de Estudos e Projetos, Fundacao Carlos Chagas Filho de Amparo a Pesquisa do Estado do Rio de Janeiro, Conselho Nacional de Desenvolvimento Cientifico e Tecnologico and the Ministerio da Ciencia, Tecnologia e Inovacao, the Deutsche Forschungsgemeinschaft and the Collaborating Institutions in the Dark Energy Survey. The Collaborating Institutions are Argonne National Laboratory, the University of California at Santa Cruz, the University of Cambridge, Centro de Investigaciones Energeticas,

Medioambientales y Tecnologicas-Madrid, the University of Chicago, University College London, the DES-Brazil Consortium, the University of Edinburgh, the Eidgenossische Technische Hochschule (ETH) Zurich, Fermi National Accelerator Laboratory, the University of Illinois at Urbana-Champaign, the Institut de Ciencias de l'Espai (IEEC/CSIC), the Institut de Fisica d'Altes Energies, Lawrence Berkeley National Laboratory, the Ludwig-Maximilians Universitat Munchen and the associated Excellence Cluster Universe, the University of Michigan, the National Optical Astronomy Observatory, the University of Nottingham, the Ohio State University, the University of Pennsylvania, the University of Portsmouth, SLAC National Accelerator Laboratory, Stanford University, the University of Sussex, and Texas A&M University.

BASS is a key project of the Telescope Access Program (TAP), which has been funded by the National Astronomical Observatories of China, the Chinese Academy of Sciences (the Strategic Priority Research Program "The Emergence of Cosmological Struc-

tures" Grant # XDB09000000), and the Special Fund for Astronomy from the Ministry of Finance. The BASS is also supported by the External Cooperation Program of Chinese Academy of Sciences (Grant # 114A11KYSB20160057), and Chinese National Natural Science Foundation (Grant # 11433005).

The Legacy Survey team makes use of data products from the Near-Earth Object Wide-field Infrared Survey Explorer (NEOWISE), which is a project of the Jet Propulsion Laboratory/California Institute of Technology. NEOWISE is funded by the National Aeronautics and Space Administration.

The Legacy Surveys imaging of the DESI footprint is supported by the Director, Office of Science, Office of High Energy Physics of the U.S. Department of Energy under Contract No. DE-AC02-05CH1123, by the National Energy Research Scientific Computing Center, a DOE Office of Science User Facility under the same contract; and by the U.S. National Science Foundation, Division of Astronomical Sciences under Contract No. AST-0950945 to NOAO.

REFERENCES

Abolfathi, B., Aguado, D. S., Aguilar, G., et al. 2018, *ApJS*, 235, 42

Allende Prieto, C., Lambert, D. L., & Asplund, M. 2001, *ApJL*, 556, L63

Aller, L. H., ed. 1984, *Astrophysics and Space Science Library*, Vol. 112, Physics of thermal gaseous nebulae

Amorín, R., Sommariva, V., Castellano, M., et al. 2014, *A&A*, 568, L8

Andrews, B. H., & Martini, P. 2013, *ApJ*, 765, 140

Atek, H., Siana, B., Scarlata, C., et al. 2011, *ApJ*, 743, 121

Baldwin, A., Phillips, M. M., & Terlevich, R. 1981, *PASP*, 93, 817

Barrera-Ballesteros, J. K., Sánchez, S. F., Heckman, T., Blanc, G. A., & Team, T. M. 2017, *ApJ*, 844, 80

Berg, D. A., Skillman, E. D., Marble, A. R., et al. 2012, *ApJ*, 754, 98

Bian, F., Kewley, L. J., & Dopita, M. A. 2018, *ApJ*, 859, 175

Blanton, M. R., Bershady, M. A., Abolfathi, B., et al. 2017, *AJ*, 154, 28

Brinchmann, J., Pettini, M., & Charlot, S. 2008, *MNRAS*, 385, 769

Bruzual, G., & Charlot, S. 2003, *MNRAS*, 344, 1000

Calzetti, D., Armus, L., Bohlin, R. C., et al. 2000, *ApJ*, 533, 682

Chabrier, G. 2003, *PASP*, 115, 763

Cid Fernandes, R., Mateus, A., Sodré, L., Stasińska, G., & Gomes, J. M. 2005, *MNRAS*, 358, 363

Dalcanton, J. J. 2007, *ApJ*, 658, 941

Davé, R., Finlator, K., & Oppenheimer, B. D. 2011, *MNRAS*, 416, 1354

Dawson, K. S., Kneib, J.-P., Percival, W. J., et al. 2016, *AJ*, 151, 44

de los Reyes, M. A., Ly, C., Lee, J. C., et al. 2015, *AJ*, 149, 79

Gao, Y.-L., Lian, J.-H., Kong, X., et al. 2017, *Research in Astronomy and Astrophysics*, 17, 041

Hsyu, T., Cooke, R. J., Prochaska, J. X., & Bolte, M. 2018, *ArXiv e-prints*, arXiv:1807.04289

Hummer, D. G., & Storey, P. J. 1987, *MNRAS*, 224, 801

Izotov, Y. I., Guseva, N. G., Fricke, K. J., & Henkel, C. 2014, *A&A*, 561, A33

Izotov, Y. I., Stasińska, G., Meynet, G., Guseva, N. G., & Thuan, T. X. 2006, *A&A*, 448, 955

Izotov, Y. I., & Thuan, T. X. 2004, *ApJ*, 616, 768

Izotov, Y. I., Thuan, T. X., & Privon, G. 2012, *MNRAS*, 427, 1229

Juneau, S., Dickinson, M., Alexander, D. M., & Salim, S. 2011, *ApJ*, 736, 104

Kakazu, Y., Cowie, L. L., & Hu, E. M. 2007, *ApJ*, 668, 853

Kauffmann, G., Heckman, T. M., White, S. D. M., et al. 2003, *MNRAS*, 341, 33

Kennicutt, Jr., R. C. 1998, *ARA&A*, 36, 189

Kewley, L. J., & Dopita, M. A. 2002, *ApJS*, 142, 35

Kewley, L. J., Dopita, M. A., Sutherland, R. S., Heisler, C. A., & Trevena, J. 2001, *ApJ*, 556, 121

Kewley, L. J., & Ellison, S. L. 2008, *ApJ*, 681, 1183

Kobulnicky, H. A., & Kewley, L. J. 2004, *ApJ*, 617, 240

Kriek, M., van Dokkum, P. G., Labb  , I., et al. 2009, *ApJ*, 700, 221

Kroupa, P. 2001, *MNRAS*, 322, 231

Lang, D. 2014, *AJ*, 147, 108

Lequeux, J., Peimbert, M., Rayo, J. F., Serrano, A., & Torres-Peimbert, S. 1979, *A&A*, 80, 155

Lian, J., Hu, N., Fang, G., Ye, C., & Kong, X. 2016, *ApJ*, 819, 73

Lian, J. H., Li, J. R., Yan, W., & Kong, X. 2015, *MNRAS*, 446, 1449

Lilly, S. J., Carollo, C. M., Pipino, A., Renzini, A., & Peng, Y. 2013, *ApJ*, 772, 119

Lin, Z., Hu, N., Kong, X., et al. 2017, *ApJ*, 842, 97

Luridiana, V., Morisset, C., & Shaw, R. A. 2015, *A&A*, 573, A42

Ly, C., Malhotra, S., Malkan, M. A., et al. 2016a, *ApJS*, 226, 5

Ly, C., Malkan, M. A., Nagao, T., et al. 2014, *ApJ*, 780, 122

Ly, C., Malkan, M. A., Rigby, J. R., & Nagao, T. 2016b, *ApJ*, 828, 67

Ly, C., Rigby, J. R., Cooper, M., & Yan, R. 2015, *ApJ*, 805, 45

Maiolino, R., Nagao, T., Grazian, A., et al. 2008, *A&A*, 488, 463

Mannucci, F., Cresci, G., Maiolino, R., Marconi, A., & Gnerucci, A. 2010, *MNRAS*, 408, 2115

Maraston, C. 2005, *MNRAS*, 362, 799

Markwardt, C. B., Swank, J. H., Barthelmy, S. D., et al. 2009, *The Astronomer's Telegram*, 2258

Nicholls, D. C., Dopita, M. A., Sutherland, R. S., et al. 2014, *ApJ*, 786, 155

Parikh, T., Thomas, D., Maraston, C., et al. 2018, *MNRAS*, 477, 3954

Pettini, M., & Pagel, B. E. J. 2004, *MNRAS*, 348, L59

Pirzkal, N., Rothberg, B., Ly, C., et al. 2013, *ApJ*, 772, 48

Raichoor, A., Comparat, J., Delubac, T., et al. 2017, *MNRAS*, 471, 3955

Salim, S., Rich, R. M., Charlot, S., et al. 2007, *ApJS*, 173, 267

Salpeter, E. E. 1955, *ApJ*, 121, 161

S  nchez, S. F., Rosales-Ortega, F. F., Jungwiert, B., et al. 2013, *A&A*, 554, A58

S  nchez, S. F., P  rez, E., S  nchez-Bl  zquez, P., et al. 2016, *RevMex*, 52, 171

Savaglio, S., Glazebrook, K., Le Borgne, D., et al. 2005, *ApJ*, 635, 260

Schlegel, D. J., Finkbeiner, D. P., & Davis, M. 1998, *ApJ*, 500, 525

Tremonti, C. A., Heckman, T. M., Kauffmann, G., et al. 2004, *ApJ*, 613, 898

Trump, J. R., Konidaris, N. P., Barro, G., et al. 2013, *ApJL*, 763, L6

Whitaker, K. E., Franx, M., Leja, J., et al. 2014, *ApJ*, 795, 104

Wright, E. L., Eisenhardt, P. R. M., Mainzer, A. K., et al. 2010, *AJ*, 140, 1868

Yuan, T.-T., Kewley, L. J., & Richard, J. 2013, *ApJ*, 763, 9

Zahid, H. J., Kewley, L. J., & Bresolin, F. 2011, *ApJ*, 730, 137

Zheng, X. Z., Bell, E. F., Papovich, C., et al. 2007, *ApJL*, 661, L41

Zou, H., Zhang, T., Zhou, Z., et al. 2018, *ApJS*, 237, 37